Materials Advances

Cite this: *Mater. Adv.*, 2021, 2, 2730

Elucidating zinc-ion battery mechanisms in freestanding carbon electrode architectures decorated with nanocrystalline $ZnMn_2O_4$†

Megan B. Sassin, *[a] Maya E. Helms,[a] Joseph F. Parker, [a] Christopher N. Chervin, [a] Ryan H. DeBlock, [a] Jesse S. Ko, ‡[b] Debra R. Rolison [a] and Jeffrey W. Long *[a]

Received 22nd February 2021,
Accepted 16th March 2021

DOI: 10.1039/d1ma00159k

rsc.li/materials-advances

Rechargeable zinc-ion batteries represent an emerging energy-storage technology that offers the advantages of low cost, use of abundant and nontoxic materials, and competitive energy content in lightly packaged forms. Nanoscale manganese oxides are among the most promising positive-electrode materials for zinc-ion cells, and their performance is further enhanced when these oxides are expressed as conformal deposits on porous carbon architectures, such as carbon nanfoam paper (CNF). We describe an "in-place" conversion of nanometric birnessite Na^+-MnOx@CNF to crystalline spinel $ZnMn_2O_4$@CNF, a manganese oxide polymorph that nominally contains sites for Zn^{2+} insertion. The $ZnMn_2O_4$@CNF cathodes are electrochemically conditioned in two-terminal cells and *ex situ* characterized using X-ray diffraction, scanning electron microscopy, energy-dispersive spectroscopy, and X-ray photoelectron spectroscopy. Despite specific Zn^{2+} insertion sites in $ZnMn_2O_4$, we demonstrate that the predominant discharge mechanism involves coupled insertion of protons and precipitation of $Zn_4(OH)_6SO_4{\cdot}xH_2O$; upon recharge, protons deinsert and $Zn_4(OH)_6SO_4$ dissolves.

Introduction

Manganese oxides (MnO*x*) have a long history as charge-storing materials in devices ranging from primary alkaline Zn/MnO_2 cells[1] to rechargeable Li-ion batteries[2] to aqueous-electrolyte electrochemical capacitors.[3–6] Interest in these oxides is on the rise because of their prospective use as positive electrodes in rechargeable Zn-ion cells *versus* a Zn metal negative electrode in Zn^{2+}-based aqueous electrolytes.[7–15] This cell chemistry inherits the advantages of the ubiquitous alkaline Zn/MnO_2 battery—low-cost, abundant components and the ability to deliver moderately high specific energy—but uses an even safer mild-pH electrolyte and is extensively rechargeable (hundreds of cycles). Other metal oxides,[16–18] sulfides,[19–21] and phosphates[22–24] are also under investigation, but MnO*x* is the most likely to transition to commercial Zn-ion batteries because of its lower cost and favorable redox potential (discharge voltage on the order of 1.3 V *vs.* Zn/Zn^{2+}).

A key advancement toward rechargeable Zn-ion batteries was the recognition that nanostructured forms of MnO*x* undergo reversible redox reactions when electrochemically cycled in mild-pH aqueous electrolytes that contain Zn^{2+} salts (*e.g.*, $ZnSO_4$). Early reports suggested that insertion/intercalation of Zn^{2+} into MnO*x*, coupled with $Mn^{3+/4+}$ redox,[16–18] provides reversible cycling to relatively high MnO*x*-specific capacity (>200 mA h g^{-1}). Other studies, however, show evidence for a multistep reaction with comparable specific capacity that involves proton insertion at MnO*x*; the coupled increase in local pH drives the precipitation of a hydrated $Zn_4(OH)_6SO_4$ at the electrode surface.[25–33] This complex discharge reaction can often be reversed by re-oxidizing MnO*x*, resulting in the release of protons and at least partial dissolution of the $Zn_4(OH)_6SO_4{\cdot}xH_2O$ precipitate. In reality, both mechanisms may be operative for a given MnO*x* material,[34] particularly those that are disordered, nanoscale, and/or porous. Optimizing the performance of MnO*x*-based positive electrodes for Zn-ion batteries requires understanding the influences of MnO*x* polymorph and electrode structure on the charge-storage mechanism, which ultimately impacts rate capability, capacity, and cycle life.[10]

Recently, we explored the electrochemical Zn-ion behavior of birnessite-like Na^+-compensated manganese oxide (Na^+–MnO*x*) distributed as ultrathin (<20 nm-thick) coatings throughout porous carbon nanofoam papers (MnO*x*@CNF).[35,36] These

---

[a] *Code 6170, Surface Chemistry Branch, U.S. Naval Research Laboratory, Washington, DC, 20375, USA. E-mail: megan.sassin@nrl.navy.mil*

[b] *Former NRC Postdoctoral Associate at the U.S. Naval Research Laboratory, USA*

† Electronic supplementary information (ESI) available: Tables of composition and structural properties; data from additional XRD, EDS; XPS, impedance, microscopy, and voltammetric analyses. See DOI: 10.1039/d1ma00159k

‡ Present address: Applied Physics Laboratory, Baltimore, MD USA.

binder-free electrodes exhibit theoretical one-electron capacity (308 mA h g_{MnO2}^{-1}) at moderate rates (1C) in 1 M $ZnSO_4$.[35] When Na_2SO_4 is added to the electrolyte, high rate (20C) operation is enabled by pseudocapacitance mechanisms. *Ex situ* characterization after conditioning at pertinent cell voltages confirms that H^+ insertion/de-insertion and subsequent $Zn_4(OH)_6SO_4{\cdot}xH_2O$ precipitation/dissolution is the dominant charge-storage mechanism for birnessite-like Na^+-MnO*x*@CNF. The reversibility of these complex multiphase reactions depend on electrolyte composition and the pore structure of the CNF-based architecture.[36]

Herein, we investigate Zn-ion charge-storage mechanisms for another MnO*x* polymorph, spinel-type $ZnMn_2O_4$, which contains tetrahedral sites that nominally accommodate Zn^{2+} insertion for divalent charge storage.[37–42] The disordered birnessite-like Na^+-MnO*x* coatings on CNFs used in our previous study are readily converted to spinel $ZnMn_2O_4$ *via* topotactic ion-exchange (Zn^{2+} for Na^+), followed by mild thermal treatment. This transformation is achieved while maintaining the nanoscale, conformal nature of the as-deposited MnO*x* at the carbon surfaces and the through-connected pore structure of the CNF (Fig. S1, ESI†). We now have the opportunity to directly compare two distinct MnO*x* polymorphs (birnessite *vs.* spinel $ZnMn_2O_4$), but expressed in identical multifunctional electrode architectures.

We first examine key electrochemical properties of $ZnMn_2O_4$@CNFs in two-terminal cells with an aqueous Zn-ion electrolyte using cyclic voltammetry, AC electrochemical impedance, and galvanostatic charge–discharge for long-term cycling. *Ex situ* characterization *via* diffraction, microscopy, and spectroscopy of electrochemically conditioned $ZnMn_2O_4$@CNFs reveals that the dominant charge-storage mechanism is similar to that of Na^+-MnO*x*@CNF, despite the presence of specific Zn^{2+} insertion sites in nanocrystalline $ZnMn_2O_4$ spinel. The charge-storage mechanism involves H^+-insertion/de-insertion and subsequent precipitation/dissolution of $Zn_4(OH)_6SO_4{\cdot}xH_2O$ at the electrified interfaces.

Results and discussion

We previously demonstrated crystal engineering of disordered birnessite Na^+-MnO*x*@CNF to crystalline spinel $LiMn_2O_4$@CNF;[43–45] here we show that this approach can be generalized to produce the Zn^{2+}-containing spinel analogue, $ZnMn_2O_4$@CNF (Fig. 1a). The first step of the process involves electroless redox deposition from aqueous permanganate to generate nanoscale Na^+-MnO*x* coatings on the carbon surfaces throughout the CNF paper.[46,47] The resulting Na^+-MnO*x*@CNFs are soaked in 1 M $ZnSO_4$ (aq) to exchange Na^+ in the lamellar MnO*x* domains with Zn^{2+}, then copiously rinsed and dried to obtain birnessite-like Zn^{2+}-MnO*x*@CNFs. The nanoscale nature of the oxide coating facilitates crystallization at a relatively mild temperature (300 °C), which minimizes particle ripening of the MnO*x* coating (Fig. 1b and c), as previously observed with $LiMn_2O_4$@CNFs.[43,44] The thermal processing step under flowing argon (low p_{O_2}) reduces Mn from its initial mixed-valent Mn oxidation state of +3.7 in birnessite Na^+-MnO*x*@CNF[43] to the expected +3 Mn oxidation state as verified by XPS (Fig. S1, ESI†).

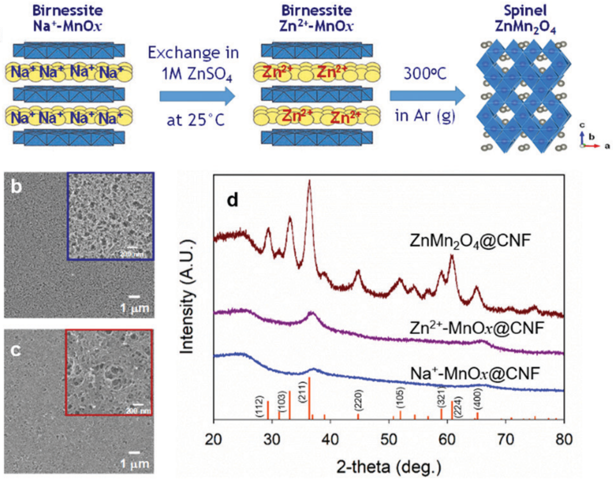

Fig. 1 (a) Schematic of in-place conversion from birnessite Na^+-MnO*x* to spinel $ZnMn_2O_4$; (b and c) Scanning electron micrographs at low and high magnification (inset) of (b) Na^+-MnO*x*@CNF and (c) $ZnMn_2O_4$@CNF; (d) X-ray diffraction patterns of Na^+-MnO*x*@CNF, Zn^{2+}-MnO*x*@CNF, and $ZnMn_2O_4$@CNF. The diffraction peaks for $ZnMn_2O_4$@CNF index to the tetragonal spinel $ZnMn_2O_4$ (ICDD# 01-071-2499).

Tracking the progress of phase conversion from birnessite Na^+-MnO*x* to spinel $ZnMn_2O_4$ with powder X-ray diffraction reveals that exchanging Na^+ for Zn^{2+} does not significantly alter the XRD pattern; both Na^+- and Zn^{2+}-MnO*x*@CNF display two broad peaks at 37 and 66° 2θ, associated with the disordered birnessite MnO*x* phase (Fig. 1d). Following thermal treatment, the disordered lamellar MnO*x* phase transforms to crystalline spinel that indexes to tetragonal $ZnMn_2O_4$ (Fig. 1d). The average crystallite size is 8 nm, as calculated from whole-pattern fitting, confirming that the coating remains nanoscale during transformation from 2D lamellar to 3D spinel.

While no other crystalline phases are observed in the $ZnMn_2O_4$@CNF XRD pattern, the retention of some minor fraction of disordered MnO*x* cannot be precluded. Elemental analysis *via* inductively coupled plasma–atomic emission spectroscopy of $ZnMn_2O_4$@CNF yields a Mn:Zn ratio of 2.4, higher than the expected 2.0 for complete conversion. If we assume that all Zn in the sample exists as $ZnMn_2O_4$, 7.7% of the Mn remains unassociated with the $ZnMn_2O_4$ phase (Table S1 and eqn (S1), ESI†). Quantitative analysis of the XPS peaks for Mn $2p_{3/2}$, Zn $2p_{3/2}$, and oxide O 1s indicates a composition of $ZnMn_{2.1}O_{3.8}$, in relative agreement with the expected $ZnMn_2O_4$ stoichiometry (Table 1 and Fig. S1, ESI†). However, we note that pair-distribution function analysis of the *in situ* crystal engineering of our disordered Na^+-MnO*x*@CNF to nanocrystalline $LiMn_2O_4$@CNF found that the first plane of MnO*x*, which forms when MnO_4^- oxidizes the carbon surface, retains a lamellar morphology that serves as the base of the 3D spinel phase. This foundational plane of MnO*x* accounts for the presence of a minor fraction of Mn remaining in a non-spinel form.[44]

Table 1 Composition and structural properties of $ZnMn_2O_4$@CNF as a function of electrochemical conditioning in 1 M $ZnSO_4$

Echem cond.	Mn:Zn[a]	S:Zn[a]	Lattice parameter[b] $a\|b\|c$	Unit cell vol.[b]	$Zn_4(OH)_6SO_4$ precipitate observed? (Method)
Uncycled	2.1	—	5.74|5.74|9.24	305	No
OCV → 1.75 V[c]	1.8	0.04	5.74|5.74|9.23	304	No
1.75 V[c]	2.0	0.08	5.74|5.74|9.19	303	No
1.3 V[c]	0.9	0.1	5.75|5.75|9.21	305	Nanoscale (?) (XPS, EDS)
0.9 V[c]	0.07	0.3	5.77|.77|9.23	308	Macroscale (XRD, SEM)

[a] Determined *via* XPS. [b] Extracted from XRD. [c] Cell held at specified voltage for 30 min.

With confirmation of successful phase transformation to spinel, we evaluated the electrochemical performance of $ZnMn_2O_4$@CNF in two-electrode cells *versus* a Zn foil anode and using 1 M $ZnSO_4$ (*aq*) electrolyte. Because as-synthesized $ZnMn_2O_4$@CNF is fully discharged with Mn in the +3 state, the electrochemical cells were first scanned to voltages positive of open circuit (~1.5 V). Somewhat surprisingly, the first positive-going voltammetric scan shows no well-defined anodic peak (Fig. 2a), as would be nominally expected for oxidation of Mn^{3+} sites to Mn^{4+}, accompanied by de-insertion of Zn^{2+} for charge balance.

To gain insight into this unexpected first-scan behaviour, we performed electrochemical impedance spectroscopy (EIS) of $ZnMn_2O_4$@CNF at 1.75 V (scanned directly from open circuit) followed by *ex situ* XPS, SEM/EDS, and XRD characterization of the conditioned electrode. The Nyquist plot reveals a high charge-transfer resistance (R_{CT}) of 26 Ω cm^2, indicative of significant impediment to multivalent ion extraction from the $ZnMn_2O_4$ domains (Fig. S2, ESI†).[42] X-ray photoelectron spectroscopy and EDS corroborate this finding, as the Zn content after 1.75 V conditioning is qualitatively similar to the uncycled $ZnMn_2O_4$@CNF (Fig. 2b, c and Fig. S3, ESI†), revealing that minimal Zn^{2+} is removed from the spinel lattice during the initial charge. This finding is in agreement with that of Manthiram and co-workers, in which they revealed Zn^{2+} is not removed from $ZnMn_2O_4$ by NO_2BF_4, a chemical mimic for electrochemical Mn oxidation.[48] Furthermore, no significant changes in lattice parameters or structure are detected by XRD between the initially charged 1.75 V sample and an uncycled $ZnMn_2O_4$@CNF (Table 1 and Fig. S4, ESI†).

The ill-defined first-scan voltammetry is consistent with other reports on the initial cycling behaviour of $ZnMn_2O_4$.[28,38] The absence of $Mn^{3+/4+}$ redox in the first positive scan is in contrast to our previous report with analogous $LiMn_2O_4$@CNF, where lattice-sited Li^+ was easily removed upon initial electrochemical oxidation of the mixed-valent Mn^{3+}/Mn^{4+} oxide.[43] Unlike $LiMn_2O_4$@CNF, the voltammetric peaks of $ZnMn_2O_4$@CNF are not well-defined in the first cycle, with only a single reduction peak at ~0.9 V observed. We attribute this reduction peak to H^+ insertion, with the supply of protons arising from the mild acidity of $Zn(H_2O)_6{}^{2+}$ in the aqueous Zn-based electrolyte.[60] The expected redox peaks become well-defined on the second and subsequent cycles, with a single anodic peak paired with two cathodic peaks (Fig. 2a). Such redox peaks are commonly attributed to extraction/insertion of Zn^{2+},[38,49] but more recently co-insertion/extraction of H^+ and Zn^{2+} into $ZnMn_2O_4$ has been proposed.[28]

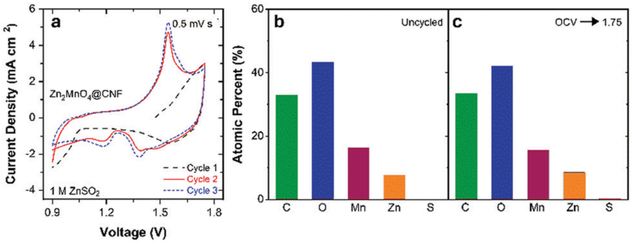

Fig. 2 (a) First three cyclic voltammograms of $ZnMn_2O_4$@CNF in 1 M $ZnSO_4$ at 0.5 mV s^{-1}. Atomic percent of each element derived from *ex situ* X-ray photoelectron spectroscopy of (b) uncycled $ZnMn_2O_4$@CNF and (c) $ZnMn_2O_4$@CNF held at 1.75 V after linearly scanning directly from OCV in 1 M $ZnSO_4$.

To elucidate the specific $ZnMn_2O_4$@CNF charge-storage mechanism in aqueous Zn^{2+}-containing electrolytes, we use a multi-pronged approach that includes EIS and *ex situ* characterization of cells conditioned at pertinent voltages. For data reported in the following sections, all $ZnMn_2O_4$@CNF-based cells are subjected to: (i) a 10-cycle voltammetric break-in; (ii) a linear scan to the voltage of interest (depicted in Fig. 3a); and (iii) potentiostating at that voltage either for 10 min prior to EIS data acquisition or for 30 min for *ex situ* characterization. Cells are quickly disassembled after voltage conditioning and the $ZnMn_2O_4$@CNF electrode is rinsed copiously with ultrapure water and dried at 50 °C under flowing N_2(g).

Electrochemical impedance spectroscopy provides insights into the charge-storage mechanism when performed as a function of applied DC voltage. Nyquist plots from this series of cells reveal significant changes in R_{CT} during charge (*e.g.*, 1.75 V, "a" in Fig. 3a)

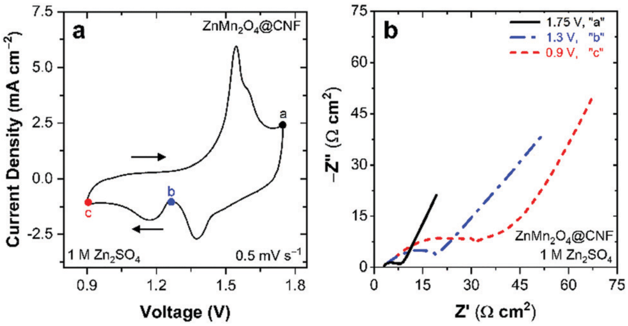

Fig. 3 (a) Cyclic voltammogram showing voltages applied for EIS and subsequent *ex situ* characterization and (b) Nyquist plot at voltages specified in (a) in 1 M $ZnSO_4$.

and discharge (*e.g.*, 1.3 V, ''b'', and 0.9 V, ''c'', in Fig. 3a). Upon charging at 1.75 V, the R_{CT} is relatively low at 5 Ω cm^2, compared to the 26 Ω cm^2 measured after initial charging from open circuit (Fig. S2, ESI†), revealing that voltammetric break-in enhances performance. Discharging from 1.75 V to 1.3 V, increases the R_{CT} 4× to 20 Ω cm^2 with a further increase to 38 Ω cm^2 after discharging at 0.9 V (Fig. 3b). We previously observed qualitatively similar results for Na^+-MnO*x*@CNF conditioned in 1 M $ZnSO_4$,[36] where R_{CT} increases significantly when fully discharged, arising from the precipitation of electronically insulating $Zn_4(OH)_6SO_4{\cdot}xH_2O$ at the electrode surface. For $ZnMn_2O_4$@CNF, the origin of the increase in R_{CT} upon discharge is attributed to either Zn^{2+} transport hindrances and/or precipitation of passivating $Zn_4(OH)_6SO_4{\cdot}xH_2O$.

We use *ex situ* X-ray diffraction to monitor the expansion/contraction of the $ZnMn_2O_4$ lattice that would arise from Zn^{2+}-insertion/extraction and the appearance of $Zn_4(OH)_6(SO_4){\cdot}xH_2O$.[27,36,39,50] All $ZnMn_2O_4$@CNFs harvested from conditioned cells show the main XRD peaks for spinel $ZnMn_2O_4$, indicating that the core crystal structure remains intact through the charge–discharge process (Fig. 4). After charging at 1.75 V, the main $ZnMn_2O_4$ peaks at 29.3, 33.1, and 36.4° 2θ shift to slightly higher 2θ compared to the uncycled $ZnMn_2O_4$@CNF, concomitant with an increase in the *a* and *b* lattice parameters and a decrease in the *c* lattice parameter and unit cell volume (Table 1). Discharging at 1.3 V does not alter either the main peak positions or corresponding cell parameters (Table 1), revealing that it is unlikely that Zn^{2+} inserts into the lattice; higher resolution synchrotron experiments are planned in the future to verify this finding.

Upon complete discharge at 0.9 V, additional diffraction peaks appear that index to $Zn_4(OH)_6(SO_4){\cdot}xH_2O$. Because of the overlap of the XRD reflections for $ZnMn_2O_4$ and $Zn_4(OH)_6SO_4{\cdot}xH_2O$, we are unable to confidently fit XRD data with respect to determining changes in lattice parameters of the $ZnMn_2O_4$ phase, precluding the determination of Zn^{2+} insertion into the lattice at 0.9 V (Table 1). The presence of $Zn_4(OH)_6SO_4{\cdot}xH_2O$ for cells discharged at 0.9 V is the likely origin of the significant increase in R_{CT} (Fig. 3b).

Ex situ SEM visualizes morphological changes in $ZnMn_2O_4$@CNF electrodes as a function of cell voltage. Energy-dispersive X-ray spectroscopy provides a means to elucidate the reaction mechanism by monitoring for the appearance of sulfur, as mapped onto the micrographs, in which sulfur serves as an elemental marker for $Zn_4(OH)_6SO_4{\cdot}xH_2O$. Uncycled $ZnMn_2O_4$@CNF provides the baseline for both morphology and sulfur content.

The exterior surface of the uncycled $ZnMn_2O_4$@CNF is featureless at low magnification and as expected, only adventitious sulfur is detected (Fig. 5a and b). Higher magnification of the exterior surface reveals the through-connected pore structure (Fig. S5, ESI†), which is also visible in the cross-section (Fig. 5c); minimal sulfur is detected in the interior of the uncycled sample (Fig. 5d).

Charging at 1.75 V does not yield any significant changes in the morphology of the exterior or interior surfaces (Fig. 5e, g and Fig. S5, ESI†), but a slight increase in sulfur content is detected (Fig. 5f and h). Upon discharging at 1.3 V, minimal-to-no-change in morphology is observed on either the exterior or the interior surfaces (Fig. 5i, k and Fig. S5, ESI†); however, an increase in sulfur content is visible in the EDS maps (Fig. 5j and l).

A significant change in morphology is observed after discharging at 0.9 V, with large plate-like precipitates visible that extensively cover the exterior surface (Fig. 5m and Fig. S5, ESI†); some of these precipitates protrude into the underlying pore structure (Fig. S5, ESI†). The cross-sectional micrograph reveals that this layer lies on top of the electrode surface and is ∼3 μm thick (Fig. 5o). A significant increase in sulfur is detected on

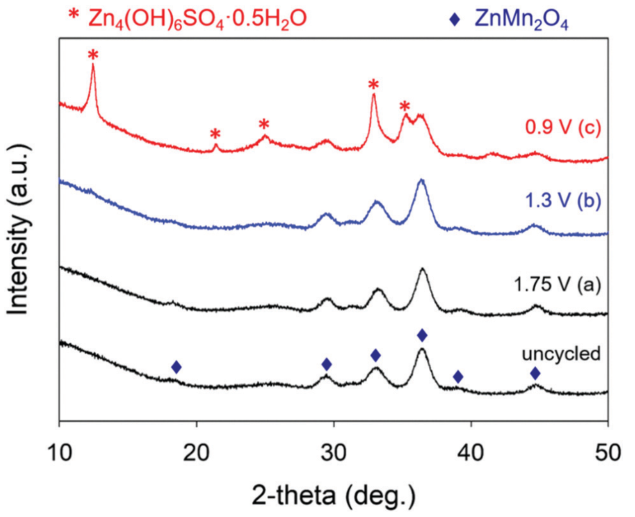

Fig. 4 X-ray powder diffraction patterns of $ZnMn_2O_4$@CNF electrodes after conditioning at specified voltages in 1 M $ZnSO_4$. The blue diamond denotes peak positions indexed to tetragonal $ZnMn_2O_4$ and the pink asterisk denotes peak positions indexed to $Zn_4(OH)_6SO_4{\cdot}5H_2O$.

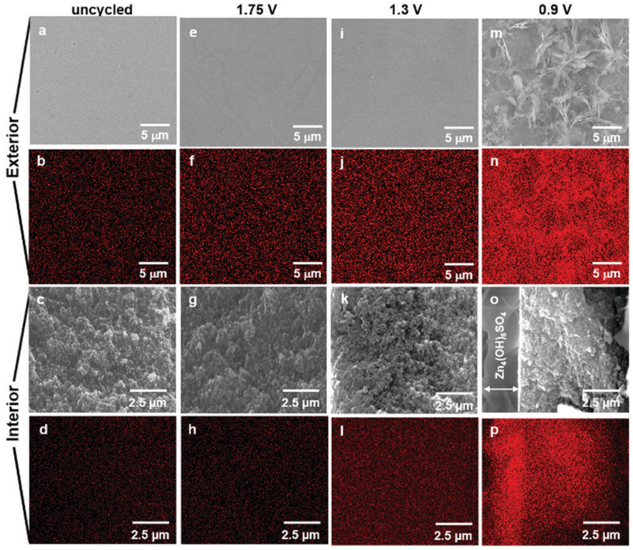

Fig. 5 Scanning electron micrographs and sulfur elemental maps of the exterior surface (top two rows) and interior surface (bottom two rows) of uncycled $ZnMn_2O_4$@CNF (a–d) and after conditioning for 30 min at 1.75 V (e–h), 1.3 V (i–l), and 0.9 V (m–p) in 1 M $ZnSO_4$.

both exterior and interior surfaces (Fig. 5n and p), but with significantly more sulfur concentrated in the 3 μm-thick exterior layer (Fig. 5p).

The SEM, EDS, and XRD results for 0.9 V-conditioned $ZnMn_2O_4$@CNF substantiate that the micrographically observed exterior layer comprises $Zn_4(OH)_6SO_4 \cdot xH_2O$. In addition to confirming the presence of sulfur, the EDS spectra show an increase in Zn and decrease in Mn (Fig. S6, ESI†) and the XRD data (Fig. 4) corroborates the presence of crystalline $Zn_4(OH)_6SO_4 \cdot xH_2O$. A similar plate-like morphology was also visible on the exterior surface for fully discharged birnessite-type Na^+-MnOx@CNF electrodes cycled in 1 M $ZnSO_4$.[36]

The presence of sulfur throughout the interior of the 0.9 V-conditioned electrode (Fig. 5p) coupled with the observation that $Zn_4(OH)_6SO_4$ crystallites are oriented orthogonally to the electrode surface, and do not completely occlude the underlying pore structure (Fig. S5, ESI†), reveals that a large fraction of the electrode volume remains accessible to the electrolyte and available to participate in the charge-storage reaction. The absence of visible $Zn_4(OH)_6SO_4 \cdot xH_2O$ precipitates in the interior voids of the $ZnMn_2O_4$@CNF stems from the fact that there is only 10% of the required Zn^{2+} for the reaction inside these pores (eqn (S2), ESI†).[36]

Tracking the atomic ratios (Mn:Zn and S:Zn) by *ex situ* XPS provides further insight into the charge-storage mechanism. The Mn:Zn ratio of uncycled $ZnMn_2O_4$@CNF is 2.1 and after conditioning at 1.75 V decreases slightly to 2, revealing a general return to the starting state after voltammetric break-in and charging (Table 1 and Fig. 6a, b). A small amount of sulfur persists after charging at 1.75 V, detectable by both XPS (S:Zn ratio of 0.08) and EDS (Fig. 5f, h and Fig. S6, ESI†), which we attribute to a patchy <7 nm-thick $Zn_4(OH)_6SO_4 \cdot xH_2O$ layer present at a level below the detection limit of XRD; this insulating coating could also be the source of the contrast differences observed in the corresponding micrograph (Fig. 5e). Discharging at 1.3 V decreases the Mn:Zn ratio to 0.9, concomitant with an increase in the S:Zn ratio to 0.10 (Table 1 and Fig. 6c). The binding energy of the S $2p_{3/2}$ peak is 168.8 eV, consistent with sulfate, indicating either that SO_4^{2-} associates at edge sites or that nanoscale $Zn_4(OH)_6SO_4 \cdot xH_2O$ is present below the detection limits of XRD. The Mn:Zn ratio decreases by over an order of magnitude to 0.07 upon discharge at 0.9 V (Table 1 and Fig. 6d), attributed to screening of the underlying $ZnMn_2O_4$ by the 3 μm-thick $Zn_4(OH)_6(SO_4) \cdot xH_2O$ overlayer (Fig. 5o). By measuring a Zn- and S-rich surface (S:Zn ratio = 0.3; Fig. 6d), the XPS data are consistent with the presence of $Zn_4(OH)_6SO_4 \cdot xH_2O$.

Although $ZnMn_2O_4$ contains specific insertion sites for Zn^{2+}, our data confirm that the dominant charge-storage mechanism for $ZnMn_2O_4$@CNF is H^+ insertion/de-insertion with subsequent precipitation/dissolution of $Zn_4(OH)_6(SO_4) \cdot xH_2O$, similar to that observed on our birnessite-like Na^+-MnOx@CNF.[36] This same reaction mechanism has been proposed for VO_2,[51,52] $V_3O_7 \cdot H_2O$,[53,54] V_2O_5,[55] NaV_3O_8,[56] $V_{10}O_{24} \cdot 12H_2O$,[57] and Co_3O_4[58] cathode materials, revealing that pH changes upon H^+ insertion/de-insertion is a general charge-storage mechanism for oxide-based materials in aqueous $ZnSO_4$ electrolytes, as recently suggested by Kundu and co-workers.[53]

Circumventing this general precipitation/dissolution process would be advantageous from a performance standpoint (*e.g.*, long-term cycling and rate), but swapping NO_3^- for SO_4^{2-} is not feasible, as the former is too oxidizing for the Zn anode. Buffering the SO_4^{2-} electrolyte, however, may be an effective strategy to suppress the precipitation of the $Zn_4(OH)_6SO_4 \cdot xH_2O$ salt and is the focus of future experiments.

A charge-storage mechanism that involves precipitation/dissolution of $Zn_4(OH)_6(SO_4) \cdot xH_2O$ on the surface of the $ZnMn_2O_4$@CNF electrode influences both the capacity and rate of Zn-ion cells; and as such, 3D electrode–architecture designs play a role in energy-storage performance. Cyclic voltammometric examination of $ZnMn_2O_4$@CNF as a function of scan rate reveals that $ZnMn_2O_4$-based redox peaks are discernible at scan rates as high as 10 mV s^{-1} (Fig. 7a). This impressive rate performance, for a nominal battery material, is due to sufficient counter-ion compensation from both an adequate volume of electrolyte within the pores and to rapid transport of ions to the $ZnMn_2O_4$ domains *via* the through-connected pore structure of the underlying CNF. A 3D design-enabled performance we have demonstrated with CNFs modified with other MnOx polymorphs.[59]

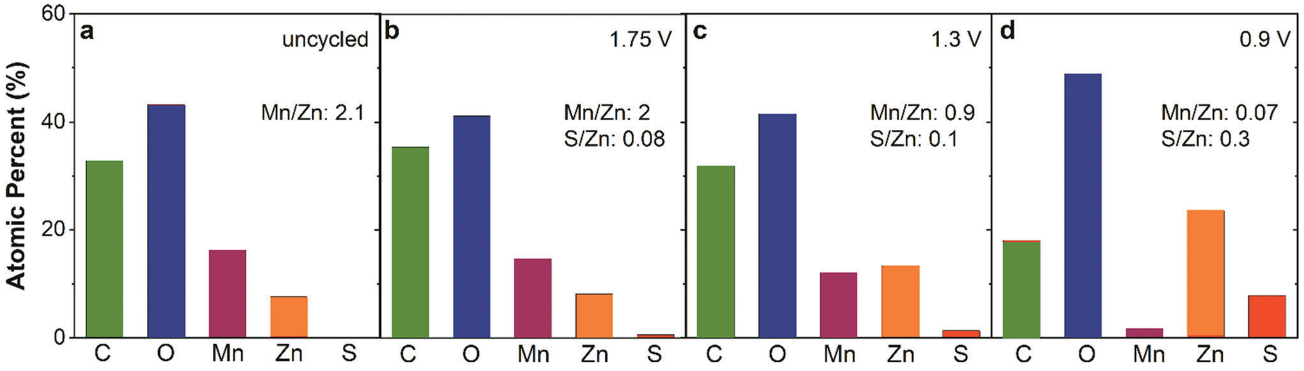

Fig. 6 Atomic percent of each element derived from *ex situ* XPS of $ZnMn_2O_4$@CNF electrodes as a function of voltage conditioning: (a) uncycled, (b) 1.75 V, (c) 1.3 V, and (d) 0.9 V in 1 M $ZnSO_4$.

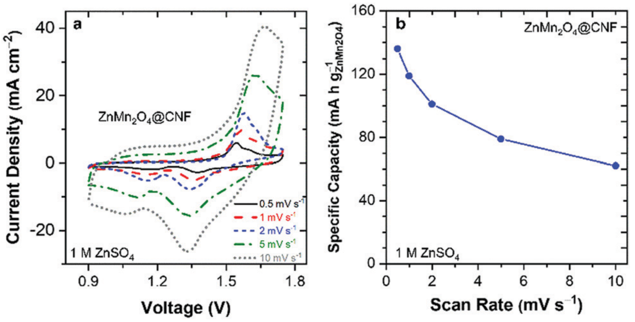

Fig. 7 (a) Cyclic voltammograms and (b) specific capacity of $ZnMn_2O_4$@CNF in 1 M $ZnSO_4$ as a function of scan rate.

A specific capacity of 119 mA h $g_{ZnMn2O4}{}^{-1}$ is delivered at 1 mV s^{-1} (Fig. 7b), on par with the 1-electron theoretical capacity of $ZnMn_2O_4$ (116 mA h g^{-1}), further confirming that the charge-storage mechanism is H^+ insertion/$Zn_4(OH)_6SO_4$ precipitation. As the scan rate increases to 10 mV s^{-1}, the capacity decreases to 62 mA h g^{-1} (Fig. 7b). The realization of theoretical specific capacity is a consequence of the 3D multifunctional electrode architecture (Fig. S7, ESI†). The 20 nm-thick $ZnMn_2O_4$ domains are well-wired to the underlying carbon current collector, as it is generated from the precursor MnO*x* phase that is deposited *via* $MnO_4{}^{-1}$ redox deposition. In this deposition, the carbon in the nanofoam serves as a sacrificial reductant, and thus the first few layers of the MnO*x* are embedded into the carbon current collector.[43,46,47] The through-connected pore volume/structure of the 3D multifunctional electrode ensures an adequate supply and rapid transport of ions to the $ZnMn_2O_4$ domains,[59] supporting rapid charge–discharge at nominally high rates (1 mV s^{-1} = 28 min charge/discharge) for a battery material. This 1-electron high-capacity at high rate is in agreement with our previous results for both crystalline spinel $LiMn_2O_4$@CNF and Na^+-birnessite-type MnO*x*@CNF, where these electrodes deliver full theoretical capacity (148 mA h g^{-1} at 2 mV s^{-1} and 308 mA h g^{-1} at 1C, respectively) when cycled in Li^+- and Zn^{2+}-containing aqueous electrolytes, respectively.[35,43]

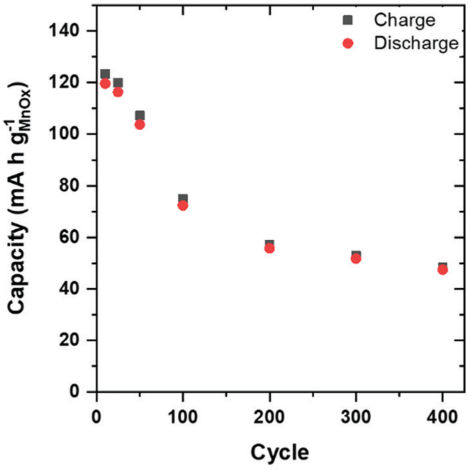

Fig. 8 Capacity *versus* cycle number for $ZnMn_2O_4$@CNF in 1 M $ZnSO_4$ at a 1C rate.

Long-term electrochemical stability is a key requirement for MnO*x*-based active materials used in aqueous Zn-ion cells. We cycle $ZnMn_2O_4$@CNF in two-terminal cells with a Zn-foil anode and 1 M $ZnSO_4$ electrolyte at 1C (136 mA h $g_{ZnMn2O4}{}^{-1}$) for 400 cycles (7 weeks). Capacity decays significantly over the first 200 cycles and plateaus from cycle 200 to 400, leading to a 50% decrease in total capacity (Fig. 8).

The mildly acidic nature of 1 M $ZnSO_4$ (aq) is known to promote reductive dissolution of MnO*x* as Mn^{3+} disproportionates to generate soluble Mn^{2+}, which could be the source of the capacity fade. To assess this hypothesis, we soaked $ZnMn_2O_4$@CNF in 1 M $ZnSO_4$ for 13 days and upon addition of potassium periodate to a portion of the solution, the electrolyte changed from colorless to magenta, indicating the presence of soluble Mn^{2+} species (Fig. S8, ESI†), confirming the disproportionation reaction resulting from the mild acidity of 1 M $ZnSO_4$. Gravimetric analysis of the $ZnMn_2O_4$@CNF after soaking in 1 M $ZnSO_4$, revealed a 6 wt% loss, leaving 35 wt% $ZnMn_2O_4$ for charge-storage.

This long-term stability problem has been previously addressed by adding Mn^{2+} (*e.g.*, 0.010–0.05 M $MnSO_4$) to the electrolyte to drive the equilibrium back toward $Mn^{3+/4+}$ oxide, resulting in extended cycle life.[38] We do not obtain such improvements when using 0.05 M $MnSO_4$ + 1 M $ZnSO_4$ in our cycling studies. For our particular electrode structure, we calculate that if 10% of the nanofoam-supported $ZnMn_2O_4$ were to dissolve, the Mn^{2+} concentration would reach 0.7 M inside the pores (eqn (S3), ESI†). This degree of dissolution likely represents an extreme condition, but reveals that 0.05 M Mn^{2+} is insufficient at suppressing the disproportionation reaction in this porous CNF architecture. In on-going experiments, we are exploring other strategies, including buffering the electrolyte,[30,60] as well as methods to form nanoscale protective coatings at the oxide surface, as previously achieved using bicarbonate electrolyte additives at $LiMn_2O_4$@CNF.[43]

Conclusions

Our ability to crystal engineer 2D lamellar birnessite-like Na^+-MnO*x* inside high surface-area CNF is extended to generate nanocrystalline $ZnMn_2O_4$@CNF. We show that despite specific lattice sites for Zn^{2+} insertion into the spinel, the dominant charge-storage mechanism of $ZnMn_2O_4$@CNF in 1 M $ZnSO_4$ remains H^+ insertion/de-insertion coupled with precipitation/dissolution of $Zn_4(OH)_6SO_4{\cdot}xH_2O$. A 50% decrease in capacity is observed over 400 cycles when cycled at 1C, which is attributed to dissolution of $ZnMn_2O_4$, the bulk of which resides in the CNF interior, *via* disproportionation of electrogenerated Mn^{3+} to Mn^{4+} and soluble Mn^{2+}.

Experimental

Chemicals and materials

Resorcinol (Sigma Aldrich, 99%), formaldehyde (Sigma Aldrich, 37 wt% in H_2O, 10–15% methanol stabilizer), sodium carbonate

(Aldrich Chemical Company, Inc., 99.5 + %), Na_2SO_4 (Sigma Aldrich, ≥99.0%), $NaMnO_4{\cdot}H_2O$ (Sigma Aldrich, ≥97%) and $ZnSO_4$ (Sigma Aldrich, ≥99.0%) were used as received. Carbon fiber papers (Lydall Technimat), cellulose acetate filters (1.2 μm pores, SterliTech Corporation), and 0.25 mm Zn foil (Alfa Aesar, 99.98% metal basis) were used as described.

$ZnMn_2O_4$@CNF synthesis

One-ply 40/500 carbon nanofoam papers (CNF) were fabricated using a previously reported protocol.[61] Briefly, the 40/500 resorcinol–formaldehyde (RF) sol was prepared by mixing 10 g resorcinol + 14.74 g formaldehyde + 0.0177 g sodium carbonate + 13.9 g water and stirring on a magnetic stir plate set at 250 rpm for 30 min, followed by a 2.5 h resting period. Carbon fiber papers (2.5 × 4.5 cm^2) were exposed to an air–ice RF plasma (Harrick PlasmaFlo PDC-FMG) for 45 min to introduce oxygen functionalities on the carbon fiber surfaces. The CFPs were then vacuum-infiltrated with the RF sol to generate RF-CFPs and placed between two glass slides with each glass slide edge secured with a mini binder clip. The glass slide assembly was then sealed in duct tape. The RF-CFPs were placed in an aluminum foil pouch with ~2 mL of water and allowed to cure under ambient conditions for 20 h, then placed in a pressure cooker (Nesco 3-in-1, Target) for 9.5 h at ''slow cook'' (~88–94 °C) and then at ''warm'' until removed. The RF-CFPs were removed from the glass slides, soaked in nanopure water and acetone, each for 1 h, and dried under ambient conditions. Pyrolysis of the RF-CFPs was performed in a tube furnace (Thermo Scientific Lindberg Blue M) under flowing argon by ramping to 1000 °C at a 1 °C min^{-1} and held at 1000 °C for 2 h to generate carbon nanofoam papers (CNFs).

Manganese oxide (birnessite-like Na^+-MnOx) was electrolessly deposited onto the ''one-ply 40/500'' CNF by soaking under vacuum in 0.1 M Na_2SO_4 for 20 h and then in 0.1 M $NaMnO_4{\cdot}H_2O$ + 0.1 M Na_2SO_4 for 20 h, generating Na^+-MnOx@CNF.[46] The Na^+-MnOx@CNF were removed from the $NaMnO_4$ solution, thoroughly rinsed with nanopure water, vacuum infiltrated with nanopure water and soaked under vacuum for 1 h; the rinse/soak process was repeated a total of three times. The Na^+-MnOx@CNF were dried at 50 °C under flowing $N_2(g)$ for 20 h.

To generate $ZnMn_2O_4$@CNF, the Na^+-MnOx@CNFs were vacuum infiltrated with 1.0 M $ZnSO_4$ solution and soaked under vacuum for 24 h, removed from the 1 M $ZnSO_4$ solution, rinsed copiously with nanopure water, and soaked in nanopure water under vacuum for 1 h, with the nanopure water rinse/soak step repeated two more times. The Zn^{2+}-MnOx@CNFs were dried at 50 °C under flowing $N_2(g)$ for 12 h. Next, the Zn^{2+}-MnOx@CNF papers were placed in a tube furnace under flowing argon, ramped to 300 °C at a rate of 2 °C min^{-1}, held at 300 °C for 4 h, and then cooled to ambient temperature before removing from the furnace.

Elemental analysis

A $ZnMn_2O_4$@CNF sample was analyzed to quantitatively determine Mn, Na, and Zn content (sent to Galbraith Laboratories, Inc.). Prior to analysis by inductively coupled plasma–atomic emission spectroscopy, the samples were dried under vacuum.

Electrochemical characterization

Prior to electrochemical tests, the $ZnMn_2O_4$@CNF electrode was vacuum-infiltrated with 1 M $ZnSO_4$ for 4 h. Two-electrode Zn-ion Swagelok cells were fabricated with a $ZnMn_2O_4$@CNF cathode (1/2″ diameter circle), a cellulose acetate filter wetted with 1 M $ZnSO_4$ as the separator, and a 0.25 mm-thick Zn foil as the anode. A Gamry REF 600 potentiostat was used to collect cyclic voltammetry, linear sweep voltammetry, chronoamperometry, and AC electrochemical impedance spectroscopy data. Cyclic voltammetry was carried out from 0.9 V to 1.75 V at scan rates of 0.5, 1, 2, 5, and 10 mV s^{-1}. *Ex situ* and EIS data on $ZnMn_2O_4$@CNF samples were generated by first doing a 10-cycle voltammetric break-in from 1.75 to 0.9 V to 1.75 V at 2 mV s^{-1}, followed by linear-scan voltammetry at 0.5 mV s^{-1} to a specified voltage (1.75 V, 1.3 V, or 0.9 V) and holding at that voltage for either 30 min for *ex situ* characterization samples or 10 min for EIS. After electrochemical conditioning, the cell voltage was terminated, the $ZnMn_2O_4$@CNF was immediately removed, rinsed well with nanopure water, and dried under flowing $N_2(g)$ for 12 h prior to analysis by XPS, XRD, and SEM/EDS.

Long-term cycling

Two-terminal Zn-ion cells with $ZnMn_2O_4$@CNF cathodes assembled as described above were galvanostatically cycled at 1C (136 mAh $g_{ZnMn_2O_4}^{-1}$) on an Arbin battery cycler.

Scanning electron microscopy

Exterior surface samples were cut with clean scissors and secured to aluminum stubs with conductive carbon tape (Ted Pella). Cross-sectional samples were prepared by immersing uncycled and conditioned $ZnMn_2O_4$@CNF samples in liquid nitrogen for 1 min, fractured with a new razor blade, and secured to a 45/90° aluminum stub with conductive carbon tape. Carbon paint was used to make an electrical connection between the exposed surface and the SEM stub, especially critical for imaging samples with electrically insulating $Zn_4(OH)_6(SO_4){\cdot}xH_2O$ precipitates. All samples were imaged with a Leo Supra 55 SEM at 20 keV equipped with an Oxford Instruments Aztec energy-dispersive X-ray detector.

X-ray photoelectron spectroscopy

Elemental analyses of the surface of the electrodes were performed using XPS (Thermo Scientific K-Alpha X-ray) equipped with a monochromatic Al Kα source (1486.68 eV) and a 400 μm elliptical spot size. High-resolution spectra over the C 1s, O 1s, Mn 2p, S 2p, and Zn 2p regions were obtained. The instrument was operated using a low-energy electron flood gun; the resulting spectra were not peak-shifted prior to quantitative analysis. Ratios of Mn:Zn and S:Zn were tracked to monitor the degree of precipitated film formation of $Zn_4(OH)_6(SO_4){\cdot}xH_2O$. The spectra were analyzed with Avantage (version 5.35).

X-ray diffraction

X-ray diffraction patterns were collected for MnO*x*@CNF and $ZnMn_2O_4$@CNF series using a 3 kW Rigaku Smartlab X-ray diffractometer operating with a Cu Kα (λ = 1.5406 Å) radiation source in continuous mode. The samples were aligned with the incident X-rays by sandwiching each sample between a glass slide and the Rigaku reference sample holder. The average crystallite sizes of selected samples were calculated using peak broadening determined from whole pattern fitting in the Rigaku PDXL analysis software. The reference structure for the pattern fitting was $ZnMn_2O_4$ (ICDD# 01-071-2499).

Conflicts of interest

The authors have no conflicts to declare.

Acknowledgements

This work was supported by the U.S. Office of Naval Research.

Notes and references

1 Y. Chabre and J. Pannetier, *Prog. Solid State Chem.*, 1995, **23**, 1–130.

2 M. M. Thackeray, *Prog. Solid State Chem.*, 1997, **25**, 1–71.

3 D. Bélanger, T. Brousse and J. W. Long, *ECS Interface Spring*, 2008, **17**, 49–52.

4 C. J. Xu, F. Y. Kang, B. H. Li and H. D. Du, *J. Mater. Res.*, 2010, **25**, 1421–1432.

5 M. Huang, F. Li, F. Dong, Y. X. Zhang and L. L. Zhang, *J. Mater. Chem. A*, 2015, **3**, 21380–21423.

6 Q. Z. Zhang, D. Zhang, Z. C. Miao, X. L. Zhang and S. L. Chou, *Small*, 2018, **14**, 1702883–1702897.

7 B. Tang, L. Shan, S. Liang and J. Zhou, *Energy Environ. Sci.*, 2019, **12**, 3288–3304.

8 X. Zeng, J. Hao, Z. Wang, J. Mao and Z. Guo, *Energy Storage Mater.*, 2019, **20**, 410–437.

9 J. Ming, J. Guo, C. Xia, W. Wang and H. N. Alshareef, *Mater. Sci. Eng., R*, 2019, **135**, 58–84.

10 M. Song, H. Tan, D. Chao and H. J. Fan, *Adv. Funct. Mater.*, 2018, **41**, 1802564.

11 L. E. Blanc, D. Kundu and L. F. Nazar, *Joule*, 2020, **4**, 771–799.

12 Y.-P. Deng, R. Liang, G. Jiang, Y. Jiang, A. Yu and Z. Chen, *ACS Energy Lett.*, 2020, **5**, 1665–1675.

13 Y. Wu, J. Fee, Z. Tobin, A. Shirazi-Amin, P. Kerns, S. Dissanayake, A. Mirich and S. L. Suib, *ACS Appl. Energy Mater.*, 2020, **3**, 1627–1633.

14 A. Dhiman and D. G. Ivey, *Batteries Supercaps*, 2020, **3**, 293–305.

15 B. Yong, D. Ma, Y. Wang, H. Mi, C. He and P. Zhang, *Adv. Energy Mater.*, 2020, 2002354.

16 J. Lee, J. B. Ju, W. I. Cho, B. W. Cho and S. H. Oh, *Electrochim. Acta*, 2013, **112**, 138–143.

17 M. H. Alfaruqi, V. Mathew, J. Gim, S. Kim, J. Song, J. P. Baboo, S. H. Choi and J. Kim, *Chem. Mater.*, 2015, **27**, 3609–3620.

18 M. H. Alfaruqi, J. Gim, S. Kim, J. Song, J. Jo, S. Kim, V. Mathew and J. Kim, *J. Power Sources*, 2015, **288**, 320–327.

19 H. Qin, Z. Yang, L. Chen, X. Chen and L. Wang, *J. Mater. Chem. A*, 2018, **6**, 23757–23765.

20 Y. Cheng, L. Luo, L. Zhong, J. Chen, B. Li, W. Wang, S. X. Mao, C. Wang, V. L. Sprenkle, G. Li and J. Liu, *ACS Appl. Mater. Interfaces*, 2016, **8**, 13673–13677.

21 H. Liang, Z. Cao, F. Ming, W. Zhang, D. H. Anjum, Y. Cui, L. Cavallo and H. N. Alshareef, *Nano Lett.*, 2019, **19**, 3199–3206.

22 G. Li, Z. Yang, Y. Jiang, C. Jin, W. Huang, X. Ding and Y. Huang, *Nano Energy*, 2016, **25**, 211–217.

23 P. Hu, T. Zhua, X. Wang, X. Zhou, X. Wei, X. Yao, W. Luo, C. Shi, K. A. Owusu, L. Zhou and L. Mai, *Nano Energy*, 2019, **58**, 492–498.

24 J. S. Ko, P. P. Paul, G. Wan, N. Seitzman, R. H. DeBlock, B. S. Dunn, M. F. Toney and J. N. Weker, *Chem. Mater.*, 2020, **32**, 3028–3035.

25 H. Pan, Y. Shao, P. Yan, Y. Cheng, K. S. Han, Z. Nie, C. Wang, J. Yang, X. Li, P. Bhattacharya, K. T. Mueller and J. Liu, *Nat. Energy*, 2016, **1**, 16039.

26 B. Lee, H. R. Seo, H. R. Lee, C. S. Yoon, J. H. Kim, K. Y. Chung, B. W. Cho and S. H. Oh, *ChemSusChem*, 2016, **9**, 2948–2956.

27 Y. Wu, K. Zhang, S. Chen, Y. Liu, Y. Tao, X. Zhang, Y. Ding, T. Hayat, A. M. Abusorrah and S. Dai, *ACS Appl. Energy Mater.*, 2020, **3**, 319–327.

28 Z. Yao, D. Cai, Z. Cui, Q. Wang and H. Zhan, *Ceram. Int.*, 2020, **46**, 11237–11245.

29 D. L. Chao, W. H. Zhou, C. Ye, Q. H. Zhang, Y. G. Chen, L. Gu, K. Davey and S. Z. Qiao, *Angew. Chem., Int. Ed.*, 2019, **58**, 7823–7828.

30 C. F. Bischoff, O. S. Fitz, J. Burns, M. Bauer, H. Gentischer, K. P. Birke, H.-M. Henning and D. Biro, *J. Electrochem. Soc.*, 2020, **167**, 020545–020553.

31 D. Wu, L. M. Housel, S. J. Kim, N. Sadique, C. D. Quilty, L. Wu, R. Tappero, S. L. Nicholas, S. Ehrlich, Y. Zhu, A. C. Marschilok, E. S. Takeuchi, D. C. Bock and K. J. Takeuchi, *Energy Environ. Sci.*, 2020, **13**, 4322–4333.

32 T. Zhang, Y. Tang, G. Fang, C. Zhang, H. Zhang, X. Guo, X. Cao, J. Zhou, A. Pan and S. Liang, *Adv. Funct. Mater.*, 2020, **3**, 2002711.

33 L. Li, T. K. A. Hoang, J. Zhi, M. Han, S. Li and P. Chen, *ACS Appl. Mater. Interfaces*, 2020, **12**, 12834–12846.

34 W. Sun, F. Wang, S. Hou, C. Yang, X. Fan, Z. Ma, T. Gao, F. Han, R. Hu, M. Zhu and C. Wang, *J. Am. Chem. Soc.*, 2017, **139**, 9775–9778.

35 J. S. Ko, M. B. Sassin, J. F. Parker, D. R. Rolison and J. W. Long, *Sustainable Energy Fuels*, 2018, **2**, 626–636.

36 J. S. Ko, M. D. Donakowski, M. B. Sassin, J. F. Parker, D. R. Rolison and J. W. Long, *MRS Commun.*, 2019, **9**, 99–106.

37 N. Zhang, F. Cheng, Y. Liu, Q. Zhao, K. Lei, C. Chen, X. Liu and J. Chen, *J. Am. Chem. Soc.*, 2016, **138**, 12894–12901.

38 X. Wu, Y. Xiang, Q. Peng, X. Wu, Y. Li, F. Tang, R. Song, Z. Liu, Z. He and X. Wu, *J. Mater. Chem. A*, 2017, **5**, 17990–17997.

39 L. Chen, Z. Yang, H. Qin, X. Zeng and J. Meng, *J. Power Sources*, 2019, **425**, 162–169.

40 J.-W. Lee, S.-D. Seo and D.-W. Kim, *J. Alloys Compd.*, 2019, **800**, 478–482.

41 L. Chen, Z. Yang, H. Qin, X. Zeng, J. Meng and H. Chen, *Electrochim. Acta*, 2019, **317**, 155–163.

42 H. Zhang, J. Wan, Q. Liu, W. He, Z. Lai, X. Zhang, M. Yu, Y. Tong and X. Lu, *Energy Storage Mater.*, 2019, **21**, 154–161.

43 M. B. Sassin, S. G. Greenbaum, P. E. Stallworth, A. N. Mansour, B. P. Hahn, K. A. Pettigrew, D. R. Rolison and J. W. Long, *J. Mater. Chem. A*, 2013, **1**, 2431–2440.

44 M. D. Donakowski, J. M. Wallace, M. B. Sassin, K. W. Chapman, J. F. Parker, J. W. Long and D. R. Rolison, *CrystEngComm*, 2016, **18**, 6035–6048.

45 J. S. Ko, M. B. Sassin, D. R. Rolison and J. W. Long, *Electrochim. Acta*, 2018, **275**, 225–235.

46 A. E. Fischer, K. A. Pettigrew, D. R. Rolison, R. M. Stroud and J. W. Long, *Nano Lett.*, 2007, **7**, 281–286.

47 M. B. Sassin, C. N. Chervin, D. R. Rolison and J. W. Long, *Acc. Chem. Res.*, 2013, **46**, 1062–1074.

48 J. C. Knight, S. Therese and A. Manthiram, *J. Mater. Chem. A*, 2015, **3**, 21077–21082.

49 S. Yang, M. Zhang, X. Wu, X. Wu, F. Zeng, Y. Li, S. Duan, D. Fan, Y. Yang and X. Wu, *J. Electroanal. Chem.*, 2019, **832**, 69–74.

50 V. Soundharrajan, B. Sambandam, S. Kim, S. Islam, J. Jo, S. Kim, V. Mathew, Y.-K. Sun and J. Kim, *Energy Storage Mater.*, 2020, **28**, 407–417.

51 Z. Li, S. Ganapathy, Y. Xu, Z. Zhou, M. Sarilar and M. Wagemaker, *Adv. Energy Mater.*, 2019, **9**, 1900237–1900246.

52 Q. Pang, H. Zhao, R. Lian, Q. Fu, Y. Wei, A. Sarapulova, J. Sun, C. Wang, G. Chen and H. Ehrenberg, *J. Mater. Chem. A*, 2020, **8**, 9567–9578.

53 D. Kundu, S. H. Vajargah, L. Wan, B. Adams, D. Prendergast and L. F. Nazar, *Energy Environ. Sci.*, 2018, **11**, 881–892.

54 P. Oberholzer, E. Tervoort, A. Bouzid, A. Pasquarello and D. Kundu, *ACS Appl. Mater. Interfaces*, 2019, **11**, 674–682.

55 Y. Dong, M. Jia, Y. Wang, J. Xu, Y. Liu, L. Jiao and N. Zhang, *ACS Appl. Energy Mater.*, 2020, **3**, 11183–11192.

56 X. Shan, S. W. Kim, A. M. M. Abeykoon, G. Kwon, D. Olds and X. Teng, *ACS Appl. Mater. Interfaces*, 2020, **12**, 54627–54636.

57 W. Liu, L. Dong, B. Jiang, Y. Huang, X. Wang, C. Xu, Z. Kang, J. Mou and F. Kang, *Electrochim. Acta*, 2019, **320**, 134565.

58 L. Ma, S. Chen, H. Li, Z. Ruan, Z. Tang, Z. Liu, Z. Wang, Y. Huang, Z. Pei, J. A. Zapiena and C. Zhi, *Energy Environ. Sci.*, 2018, **11**, 2521–2530.

59 M. B. Sassin, C. P. Hoag, B. T. Willis, N. W. Kucko, D. R. Rolison and J. W. Long, *Nanoscale*, 2013, **5**, 1649–1657.

60 M. Mateos, N. Makivic, Y.-S. Kim, B. Limoges and V. Balland, *Adv. Energy Mater.*, 2020, **10**, 2000332.

61 J. C. Lytle, J. M. Wallace, M. B. Sassin, A. J. Barrow, J. W. Long, J. L. Dysart, C. H. Renninger, M. P. Saunders, N. L. Brandell and D. R. Rolison, *Energy Environ. Sci.*, 2011, **4**, 1913–1925.